CSIRO PUBLISHING

Australian Journal of Physics

Volume 52, 1999

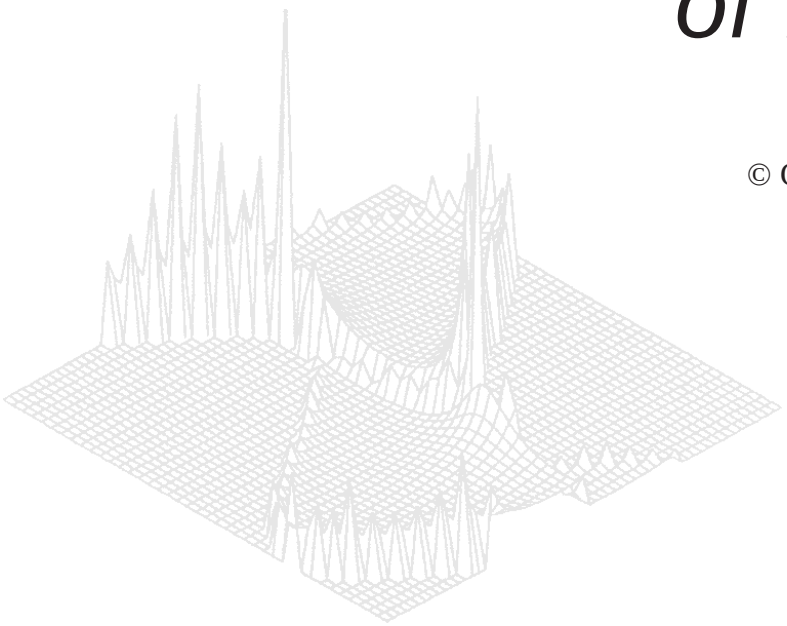

A journal for the publication of
original research in all branches of physics

www.publish.csiro.au/journals/ajp

All enquiries and manuscripts should be directed to
Australian Journal of Physics
CSIRO PUBLISHING
PO Box 1139 (150 Oxford St)
Collingwood Telephone: 61 3 9662 7626
Vic. 3066 Facsimile: 61 3 9662 7611
Australia Email: peter.robertson@publish.csiro.au

Published by **CSIRO** PUBLISHING
for CSIRO Australia and
the Australian Academy of Science

Aust. J. Phys., 1999, **52**, 205–25

Evolution of Ferromagnetism in $LaMnO_{3+\delta}$*

Michihito Muroi and Robert Street

Special Research Centre for Advanced Mineral and Materials Processing,
Department of Physics, University of Western Australia,
Nedlands, WA 6907, Australia.

Abstract

An extensive study has been made of the magnetic properties of $LaMnO_{3+\delta}$ with finely tuned hole concentrations, x (=2δ), ranging between $0{\cdot}08$ and $0{\cdot}15$. As x increases in the range studied, the spontaneous magnetisation at low temperature increases from only about 20% to almost 100% of the value for full polarisation of Mn spins, and the coercivity H_c decreases by more than an order of magnitude, e.g. from $4{\cdot}2$ kOe to 120 Oe at 5 K. The magnetic ordering temperature T_c takes a minimum at $x = x_c \sim 0{\cdot}12$. For $x < x_c$, the inverse susceptibility shows a marked decrease as T_c is approached from above. Measurements of minor hysteresis loops for the sample with $x = 0{\cdot}08$ show that magnetisation is reversible with respect to field changes except near H_c. These observations are discussed in terms of a two-phase exchange coupling (TPEC) model in which it is assumed that at low temperature the system separates into two phases, a hole-free antiferromagnetic phase and an optimally doped ferromagnetic phase, and the two phases are coupled through superexchange interactions at the interface.

1. Introduction

Mixed-valence perovskite manganites have recently attracted a great deal of attention because of their intriguing properties, such as the colossal magnetoresistance (CMR) effect (Searle and Wang 1970; Kusters *et al.* 1989; von Helmolt *et al.* 1993; Chahara *et al.* 1993; Urushibara *et al.* 1995) and field-induced structural changes (Asamitsu *et al.* 1996), which are believed to arise from strong coupling between the charge, spin and orbital degrees of freedom. Although a major focus of the research activity has been the CMR effect, their magnetic properties are of great interest in their own right. An earlier extensive neutron diffraction (ND) study of $La_{1-x}Ca_xMnO_3$ by Wollan and Koehler (1955) already revealed that the system exhibits a rich variety of magnetic structures, depending on the nominal hole concentration x. They found five different types of magnetic structure: the A-type, B-type, CE-type, C-type and G-type, which appear successively as x increases from 0 to 1. Of these, only the B-type structure, observed for $\sim 0{\cdot}2 < x < \sim 0{\cdot}4$, corresponds to a ferromagnet, while the others correspond to antiferromagnets having different spin configurations.

Since ferromagnetism evolves in the antiferromagnetic parent compound $LaMnO_3$, the understanding of the magnetic structure in the low-x region

* Refereed paper based on a contribution to the International Workshop on the Colossal Magnetoresistance (CMR) Effect, held at the University of Melbourne, 8–11 June 1998.

 10.1071/PH98059 0004-9506/99/020205$10.00

($x < 0{\cdot}2$) is of fundamental importance. From their ND data, Wollan and Koehler (1955) suggested two possibilities, (i) a mixture of antiferromagnetic (AF) and ferromagnetic (FM) phases, and (ii) homogeneous spin canting, but favoured the first interpretation based on the fact that the intensities of the ND peaks for the FM component decrease with increasing field while those for the AF component are field-independent. Goodenough (1955) considered the doping dependence of the magnetic structure from the viewpoint of chemical bonding, and also predicted an AF–FM two-phase mixture for $x < 0{\cdot}1$. On the other hand, de Gennes (1959) applied a tight-binding approach to the double exchange model (Zener 1951), and arrived at the conclusion that in the low-x region a competition between the double exchange and superexchange interactions led to a spin-canted structure. Since this theoretical work by de Gennes, spin canting has been a widely accepted magnetic structure in the low-x region. However, a number of experimental studies have recently been carried out which seem to be consistent with the original two-phase picture. For example, for low values of x, the zero-field-cooled magnetisation versus temperature curve shows a peak below T_c, which was interpreted as an indication of random freezing of FM clusters at low temperature (Ju and Sohn 1997; Töpfer and Goodenough 1997); an inelastic-neutron-scattering study has shown that two spin wave branches coexist in $La_{0{\cdot}95}Ca_{0{\cdot}05}MnO_3$, one having a strongly anisotropic character and the other having an isotropic character, and that the transverse Mn spin components define a finite FM correlation length of 8–10 Å (Hennion *et al.* 1997).

To gain further insight into the magnetic structure in the low hole concentration region, we have undertaken a systematic study of the magnetic properties of $LaMnO_{3+\delta}$. We chose the $LaMnO_{3+\delta}$ system*, rather than cation-substituted systems such as $La_{1-x}Ca_xMnO_3$ and $La_{1-x}Sr_xMnO_3$, for the following reasons: first, the hole concentration is determined by only one parameter, δ, which in turn can be controlled by changing only one variable, e.g. temperature. Second, since the cation ratio is fixed, all the samples can be prepared from one batch. One may thus expect better controllability of the hole concentration. Although extensive studies have already been made of the $LaMnO_{3+\delta}$ system (Töpfer and Goodenough 1997; Ritter *et al.* 1997), in these studies the hole concentration was changed over a wide range at relatively large intervals. In our experiment, on the other hand, we prepared a series of samples with finely tuned hole concentrations in a narrower range ($0{\cdot}08$–$0{\cdot}15$), taking advantage of the better controllability mentioned above, and investigated their magnetic properties in depth. Our study is thus complementary to the earlier ones.

The experimental results presented in this paper include susceptibility versus temperature curves measured both in high and low fields, sets of hysteresis loops measured at various temperatures, and minor hysteresis loops measured by reversing the field sweep at various points of the major demagnetisation curve. The results strongly suggest that the materials having low hole concentrations are composed of an AF phase and a FM phase, as originally proposed and

* In $LaMnO_{3+\delta}$ the oxygen nonstoichiometry is actually accommodated in the form of cation defects (Kuo *et al.* 1989; Van Roosmalen *et al.* 1994); it is therefore more accurate to express the chemical formula of the system as $La_{1-\alpha}Mn_{1-\alpha}O_3$ with $\alpha = \delta/(3+\delta)$. However, since the conversion is straightforward, we use the simpler formula $LaMnO_{3+\delta}$, and refer to the hole concentration as x, which is equal to 2δ, throughout this paper.

confirmed recently. However, the spin-glass-like magnetic structure in which FM clusters are randomly frozen in an AF matrix at low temperature (Ju and Sohn 1997; Töpfer and Goodenough 1997) also fails to provide consistent explanations of the results. We discuss the results in terms of a two-phase exchange coupling (TPEC) model in which it is assumed that the AF matrix is coupled with the FM clusters through superexchange interactions at the interfaces, thereby providing effective uniaxial anisotropy to the FM clusters. We have also carried out Monte Carlo computer simulations based on the TPEC model, the results of which are shown to qualitatively reproduce various experimental observations.

2. Experimental Results

Polycrystalline samples of $LaMnO_{3+\delta}$ were prepared by a standard solid-state reaction method. Stoichiometric amounts of La_2O_3 and MnO_2 were added to ethanol and mixed thoroughly in a ball mill. The powder was then dried and fired in air at 1200°C for 20 hours. The reacted powder was ground and fired again under the same conditions as above. This process of firing and grinding was repeated four times to achieve good homogeneity. The powder was then pressed into pellets and sintered in air at 1450°C for 5 hours. All the pellets were prepared from a single batch and sintered at the same time. Groups of pellets were subsequently heated in air to different temperatures between 1000 and 1400°C, annealed for 20 hours and quenched into liquid nitrogen. (The annealing time was reduced to 10 hours for temperatures higher than 1200°C to avoid excessive grain growth.)

X-ray diffraction (XRD) measurements showed that all the samples had single-phase perovskite structures with either the orthorhombic or rhombohedral symmetries. Microstructure was observed under a scanning electron microscope, and the grain size was found to be in the range 2–5 μm, with the average grain size increasing slightly with annealing temperature T_a. Magnetisation measurements (temperature dependence and hysteresis loops) were made using a SQUID magnetometer.

Fig. 1 shows the annealing temperature dependence of the hole concentration x, which was determined from the weight changes during heat-treatment using the relationship $x = 2\delta$; $\delta = 0{\cdot}04$ was assumed for $T_a = 1400$°C on the basis of literature data (Yao *et al.* 1995). It can be seen that x decreases monotonically with increasing T_a and that the rate of decrease slows down as T_a increases, consistent with published results (Kuo *et al.* 1989). Although there is uncertainty about the absolute value of x, amounting to $\pm 1\%$, Fig. 1 indicates that the hole concentration is reasonably well controlled, as intended. In the experimental data presented below, we use the values of x estimated by fitting the data points to a fourth-order polynomial, indicated by the solid curve in Fig. 1. (For simplicity, the values quoted are rounded to the nearest multiples of $0{\cdot}005$.)

In Fig. 2 the lattice constants, determined from the XRD data, are plotted as functions of x (filled symbols). The data are consistent with the two sets of published results (Van Roosmalen *et al.* 1995; Töpfer and Goodenough 1997) included in the same graph (open symbols), and show that the orthorhombicity decreases with increasing x and the structure becomes rhombohedral at $x \sim 0{\cdot}15$. However, the two-phase region around $x = 0{\cdot}15$, as reported by Töpfer and Goodenough (1997), was not observed in our experiment; this difference may

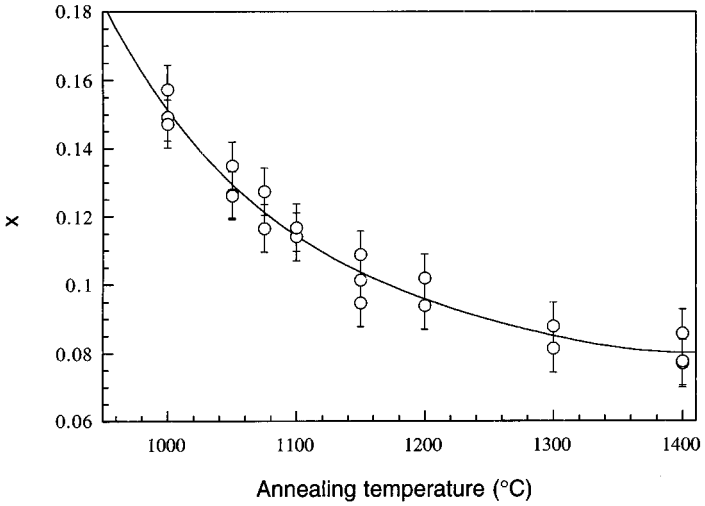

Fig. 1. Hole concentration x $(=2\delta)$ of $LaMnO_{3+\delta}$ samples plotted as a function of annealing temperature. The values of x were estimated from the weight changes during heat-treatment. The data points are fitted to a fourth-order polynomial (solid curve).

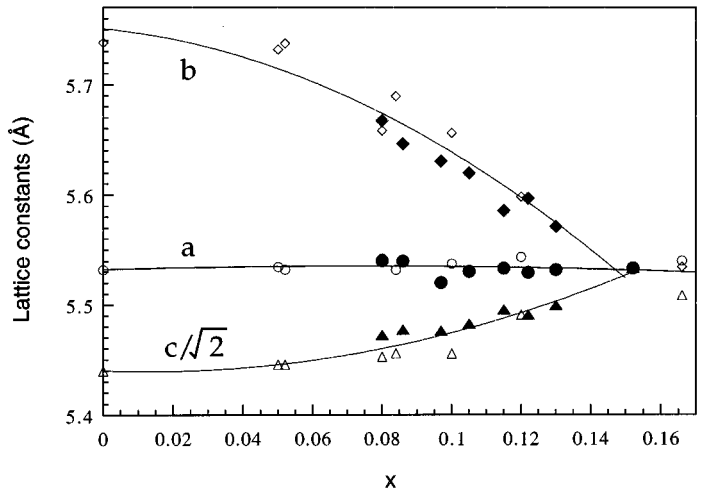

Fig. 2. Lattice constants of $LaMnO_{3+\delta}$ samples plotted as functions of x $(=2\delta)$. Filled symbols: this work. Open symbols: after Van Roosmalen *et al.* (1995) and Töpfer and Goodenough (1997).

possibly reflect the difference in the cooling rate during the final stage of sample preparation. (We did find two phases in a sample prepared by slowly cooling in air from 1400°C.)

In the left column of Fig. 3 the susceptibility χ versus temperature T curves are shown for various values of x; each graph contains the field-cooled (FC) and zero-field-cooled (ZFC) branches measured in 100 Oe and the FC branch

measured in 70 kOe. Apart from minor details, the low-field FC curves are typical of ferromagnets, with a sharp rise in χ near T_c, which is defined here as the temperature corresponding to the inflection point of the curve. The low-field ZFC curves, on the other hand, show peaks near T_c, and χ is much smaller than in the FC case at low temperature, particularly for smaller x. A similar feature was observed in the same system (Töpfer and Goodenough 1997), as well as in $La_{0\cdot8}Ca_{0\cdot2}MnO_3$ (Ju and Sohn 1997), and was interpreted as spin-glass magnetic behaviour resulting from random freezing of FM spin clusters. The FM transitions are much broader in 70 kOe, with significant tailing on the high-temperature side of the χ versus T curves.

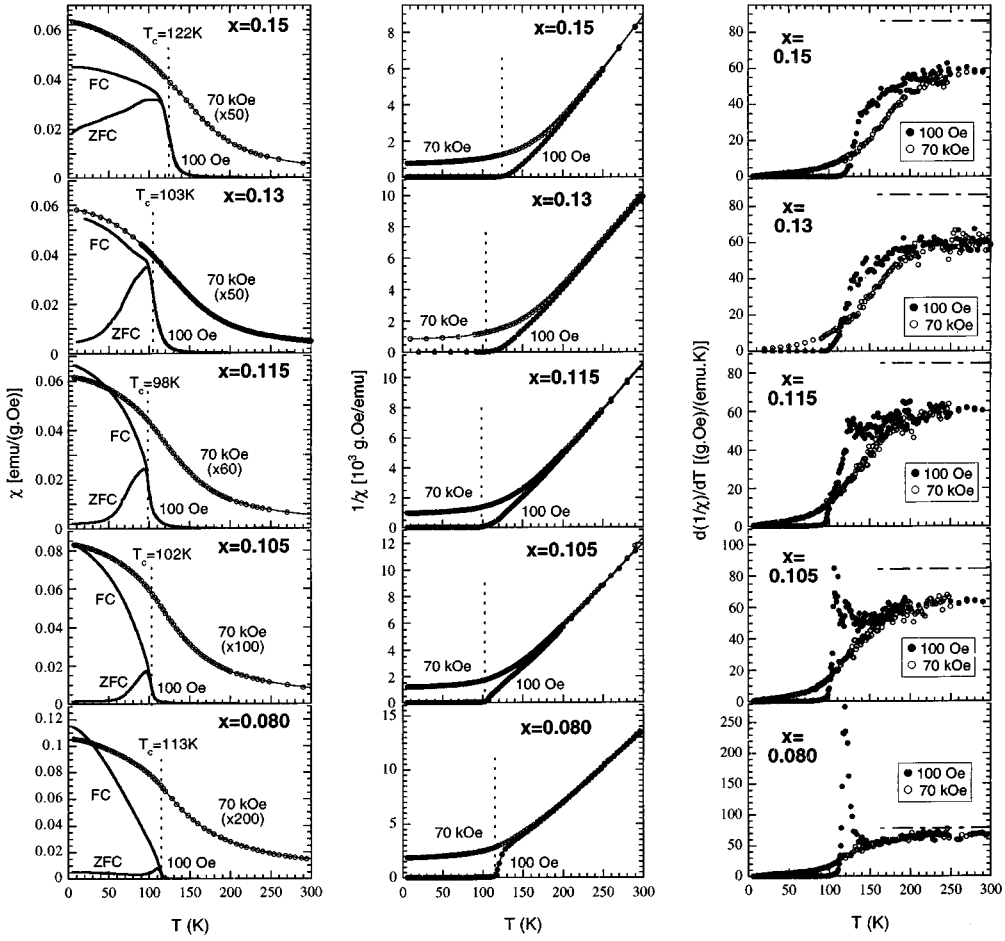

Fig. 3. Plots of χ versus T curves (left column), $1/\chi$ versus T curves (middle column), and $\mathrm{d}(1/\chi)/\mathrm{d}T$ versus T curves (right column) for various values of x.

The corresponding inverse susceptibility $(1/\chi)$ versus T curves are shown in the middle column of Fig. 3. The low-field curves for $x = 0\cdot15$ and $0\cdot13$ are typical of ferromagnets: the curves are roughly linear at high temperature and show upward curvature near T_c. The low-field curves for $x \leq 0\cdot115$, however,

exhibit an anomaly near T_c; that is, the curvature of the $1/\chi$ versus T curves changes from upward to downward as T_c is approached from above. This feature, which becomes more pronounced as x decreases, is indicated more clearly by the peaks in the $d(1/\chi)/dT$ versus T plots shown in the right column of Fig. 3. The onset temperature of this anomaly (T_0) may be defined as the temperature corresponding to the local minimum of the $d(1/\chi)/dT$ versus T plot. For $0{\cdot}08 \leq x \leq 0{\cdot}115$, T_0 is in the range 135–145 K, values which are close to the Néel temperature T_N of $LaMnO_3$ (Matsumoto 1970). The $1/\chi$ versus T curves measured in 70 kOe are qualitatively similar and no anomaly is found regardless of x.

The effective Bohr magneton numbers p_{eff}, derived from the slope of the $1/\chi$ versus T curve, $d(1/\chi)/dT$, assuming the Curie–Weiss law, range from $5{\cdot}3\ \mu_B$ for $x = 0{\cdot}08$ to $5{\cdot}7\ \mu_B$ for $x = 0{\cdot}15$ (at 300 K), values which are much larger than those expected for a mixture of Mn^{3+} ($4{\cdot}9\ \mu_B$) and Mn^{4+} ($3{\cdot}9\ \mu_B$), particularly for larger x. [The values of $d(1/\chi)/dT$ expected for the appropriate Mn^{3+}/Mn^{4+} mixtures are indicated by the horizontal dash–dot lines in the $d(1/\chi)/dT$ versus T plots in Fig. 3.] For any value of x the $d(1/\chi)/dT$ versus T plot for $H = 70$ kOe lies below that for $H = 100$ Oe over a certain temperature range above T_c, and this temperature range widens as x increases. These facts indicate that FM clusters are present above T_c, that the cluster size increases with magnetic field, and that the effect of magnetic field is stronger for larger x.

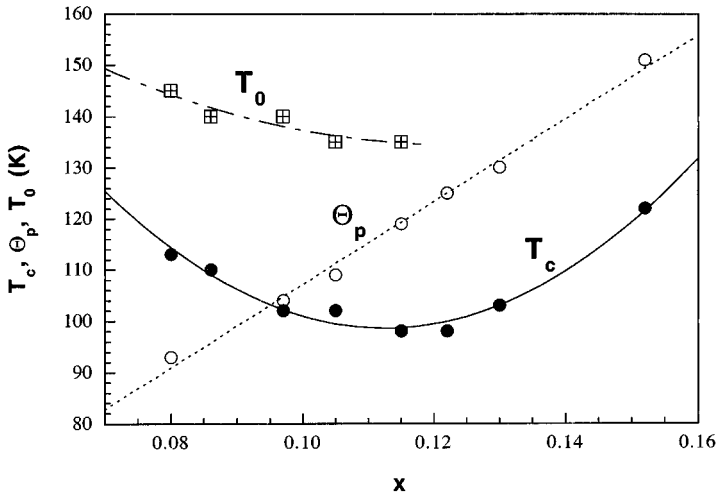

Fig. 4. Three characteristic temperatures, T_c, T_0 and Θ_p, plotted as functions of x. The definitions of T_c, T_0 and Θ_p are described in the text.

Fig. 4 summarises the x dependence of three characteristic temperatures: T_c and T_0, as defined above, and the paramagnetic Curie temperature Θ_p defined as the temperature where the tangent of the $1/\chi$ versus T curve at 300 K intersects the T-axis. It can be seen that Θ_p is almost linear in T, showing that the overall strength of FM interactions increases in proportion to x. The temperature T_0 tends to decrease slightly with increasing x in the range $0{\cdot}08 \leq x \leq 0{\cdot}115$; T_0 is not defined for $x > 0{\cdot}115$. The temperature T_c takes a minimum, 98 K, at $x \sim 0{\cdot}12$.

This is inconsistent with the de Gennes (1959) model, which predicts that the temperature at which spontaneous magnetisation appears (T_c for higher x or T_1, the onset temperature of spin canting, for lower x) decreases monotonically with decreasing x. Furthermore, for any value of x between $0{\cdot}08$ and $0{\cdot}15$, no kink is observed in the $1/\chi$ versus T curve, which according to the de Gennes model should appear at T_N for lower values of x. The absence of a purely AF phase has also been verified by ND studies on $LaMnO_{3\cdot025}$ (Ritter *et al.* 1997) and $La_{0\cdot96}Sr_{0\cdot04}MnO_3$ (Kawano *et al.* 1996): in both studies the diffraction peaks corresponding to FM and AF components were found to appear at the same temperature.

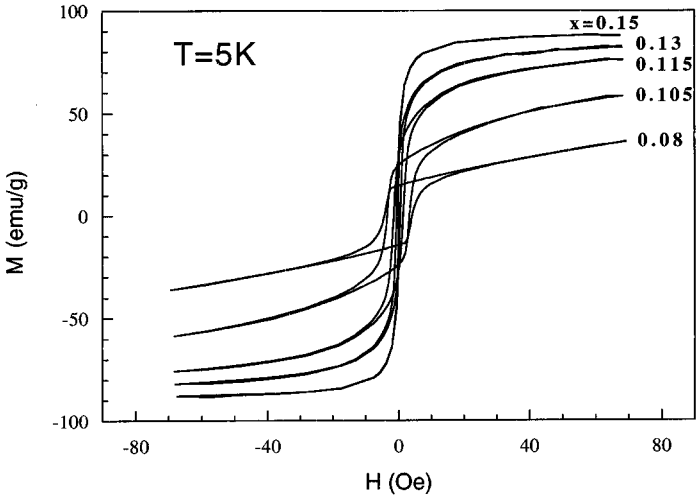

Fig. 5. Hysteresis loops measured at 5 K for $LaMnO_{3+\delta}$ samples having various values of x ($=2\delta$).

Fig. 5 shows the hysteresis loops measured at 5 K for various values of x. The hysteresis loop for $x = 0{\cdot}15$ is characterised as soft magnetic behaviour: the coercivity H_c is only about 100 Oe, and the magnetisation saturates at a relatively low field of about 10 kOe. As x decreases, H_c progressively increases and the spontaneous magnetisation M_s decreases. At the same time, the magnetisation becomes more difficult to saturate: for $x = 0{\cdot}08$ there is no indication of saturation even at 70 kOe.

The variations of M_s and H_c with x are shown in Fig. 6; M_s was determined by linear extrapolation of the data points for $40 \leq H \leq 70$ kOe to $H = 0$. (We attempted to apply standard Arott plots to determine M_s, which did not give consistent values of M_s.) As x increases from $0{\cdot}08$ to $0{\cdot}15$, M_s increases from only about 20% to almost 100% of the value for full polarisation of the Mn spins, while H_c decreases from $\sim 4{\cdot}3$ kOe to $\sim$100 Oe. Note that M_s is not linear in x but increases much more abruptly in the range of x studied. This is again inconsistent with the de Gennes model, which predicts $M_s \propto x$. For all values of x, H_c increases with decreasing temperature, as can be seen in Fig. 7, where H_c is plotted as a function of temperature. However, for lower values of x the increase in H_c shows an unexpected slowdown at the lowest temperature, suggesting a change in the magnetisation reversal mechanism.

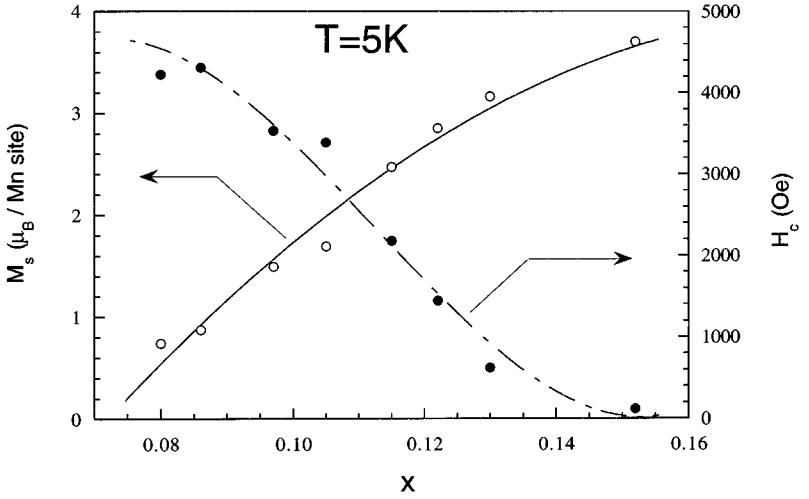

Fig. 6. Spontaneous magnetisation M_s and coercivity H_c, both at 5 K, plotted as functions of x.

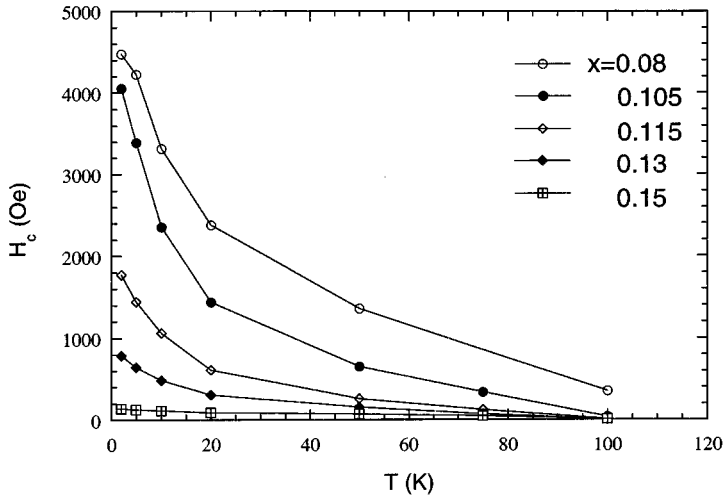

Fig. 7. Coercivity H_c plotted as a function of temperature for various values of x.

In Fig. 8 the hysteresis loops measured at various temperatures are shown for three representative values of x; the curves in the low field region, surrounded by dotted rectangles in the left-hand graphs, are expanded in the right-hand graphs. The hysteresis loops for $x = 0{\cdot}15$ show characteristics of soft ferromagnets. The saturation field and H_c are low, as already mentioned. Here M_s is nearly constant for $T < \sim T_c/2$ and then decreases as T increases towards T_c. It is noted that significant curvature is obvious even at 150 K, a temperature well above $T_c = 122$ K. This again indicates the existence of spin clusters above T_c.

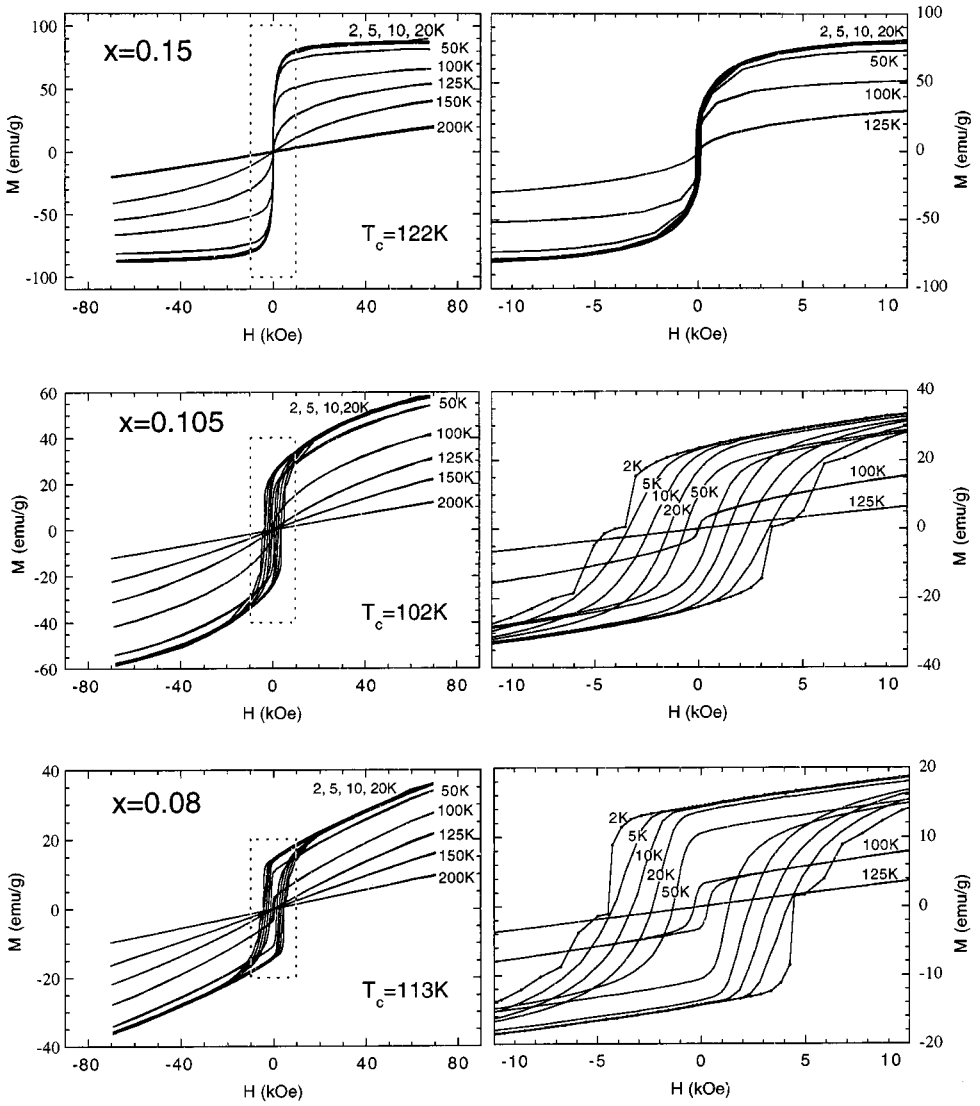

Fig. 8. Hysteresis loops measured at various temperatures for three values of x. The low-field regions surrounded by dotted rectangles in the left-hand graphs are expanded in the right-hand graphs.

The hysteresis loop for $x = 0{\cdot}105$ narrows continuously with increasing temperature, reflecting the large temperature dependence of H_c (Fig. 7). The demagnetisation curves in the region $H > 0$, however, are almost identical for $T < 50$ K and, as the temperature increases in the range $50\ \mathrm{K} < T < T_c = 102\ \mathrm{K}$, shift towards the H-axis without changing the shape. This implies that the magnetisation consists of two components: one having a field dependence roughly represented by the M versus H curve at 100 K and no temperature dependence, and the other having no field dependence and a temperature dependence similar to that for a normal ferromagnet. The hysteresis loop at $T = 2$ K shows anomalous step-like decreases

in M near $3{\cdot}5$ and $5{\cdot}5$ kOe. This anomaly is symmetrical; that is, the steps appear at the same $|H|$, regardless of the direction of field sweep. It is also reproducible with respect to repeated measurements after heating up the sample to above T_c.

The hysteresis loops for $x = 0{\cdot}08$ show the same qualitative features as those for $x = 0{\cdot}105$. However, M_s is lower, H_c is higher and M is more difficult to saturate than in the case of $x = 0{\cdot}105$.

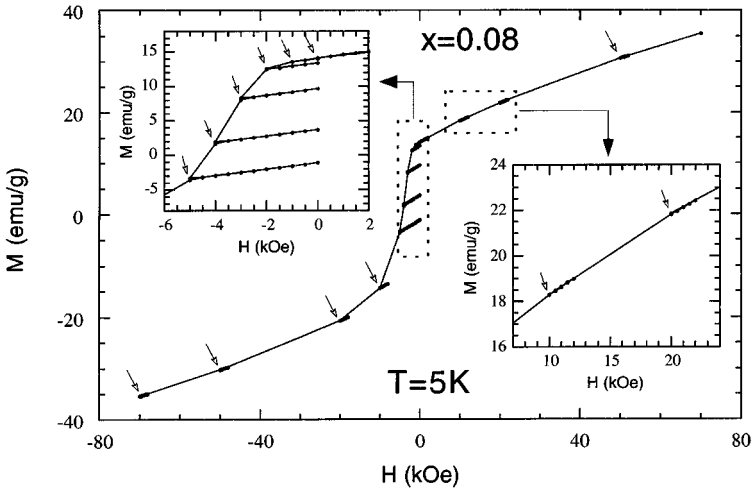

Fig. 9. Demagnetisation curve, together with minor hysteresis loops, for the sample with $x = 0{\cdot}08$. The regions surrounded by dotted rectangles are expanded in the insets. The procedure of the measurement is described in the text.

Fig. 9 shows the demagnetisation curve, together with minor hysteresis loops, measured at 5 K for $x = 0{\cdot}08$; the two regions surrounded by dotted rectangles are expanded in the insets. The procedure of the measurement is as follows: (i) stop the field sweep at various points of the demagnetisation curve H_0, marked by arrows in Fig. 9; (ii) increase the field by ΔH; (iii) decrease the field back to H_0. Here ΔH was fixed at 2 kOe except in the region $-5 \leq H \leq -1$ kOe, where the field was increased up to zero. Within each minor loop, data were collected at an interval of 500 Oe for both increasing and decreasing field. It can be seen that in the regions $H \geq -0{\cdot}1$ kOe and $H \leq -50$ kOe the minor loops coincide with the main demagnetisation curve. This means that magnetisation in these regions consists almost entirely of a reversible component. In addition, the values of M at H_0 before and after field cycling in each minor loop are almost identical, showing that the rate of magnetic relaxation is very small. In the field region near H_c ($-10 \leq H \leq -2$ kOe), however, deviation of the minor loops from the main demagnetisation curve is obvious; that is, magnetisation in this region consists of reversible and irreversible components. In the region very close to H_c ($-5 \leq H \leq -3$ kOe), the values of M at H_0 are smaller after field cycling than before field cycling, corresponding to increased rates of magnetic relaxation.

3. Discussion and Conclusions

In this section we discuss the experimental observations described above in terms of a two-phase exchange coupling (TPEC) model in which the following

assumptions are made: (i) for small x the system separates into two phases at low temperature, a hole-free AF insulating phase and an FM phase with the optimal hole concentration $x = 0{\cdot}25$–$0{\cdot}3$; (ii) the hole-rich FM regions are formed near, and are bound to, the cation vacancies each having an effective charge of $-3e$; and (iii) the two phases couple through superexchange interactions at the interface. We further assume that the magnetic interactions within FM regions are isotropic; that is, the FM ordering is three-dimensional. Considering that each cation vacancy provides three holes to the system, the local hole concentration will be optimised if the three holes are shared by about ten Mn clusters, corresponding to a FM region consisting of one to two basic perovskite unit cells.

These assumptions are contradictory to the expectation that holes doped in an A-type antiferromagnet might have a longer localisation length in the *ab*-plane because of the parallel alignment of the Mn spins, which makes the hopping of holes between neighbouring Mn sites easier. [An extreme of this view is the 'free-carrier' assumption introduced by de Gennes (1959).] The validity of this expectation, however, is not obvious, considering the following factors. First, the doped holes tend to be bound to the acceptors (cation vacancies in $LaMnO_{3+\delta}$ or A^{2+} ions in $La_{1-x}A_xMnO_3$) because of the lower Coulomb potential; electronic screening is much less effective in oxides than in usual metals, particularly at low doping levels. Second, the tendency of the holes to form polarons is intrinsically strong in manganites, as is evidenced by the insulating behaviour above T_c even for higher hole concentrations. Third, Jahn–Teller distortion will be locally suppressed, or at least diminished, near the Mn^{4+} ions, i.e. the local crystal structure becomes more isotropic. All these factors, which are neglected in the free-carrier model (de Gennes 1959), favour the formation of small 3D FM clusters over the delocalisation of holes within the *ab*-plane. (The cost in kinetic energy by reducing the localisation length in the *ab*-plane could be overcompensated by the gain in Coulomb energy and the gain in kinetic energy by delocalising holes along the *c*-axis within the FM clusters.) It is difficult, however, to determine from quantitative calculations which view is more reasonable; we instead justify our assumptions based on the result of an inelastic-neutron-scattering study on $La_{0{\cdot}95}Ca_{0{\cdot}05}MnO_3$ (Hennion *et al.* 1997), which indicates the coexistence of an anisotropic (A-type) AF phase and an isotropic FM phase having an FM correlation length of 8–10 Å in all directions.

In $LaMnO_{3+\delta}$ the cation vacancy concentration $[=2\delta/(3+\delta)]$ increases from $0{\cdot}013$ to $0{\cdot}024$, and the average separation between the vacancies decreases from $13{\cdot}0$ Å to $10{\cdot}6$ Å as x increases from $0{\cdot}08$ to $0{\cdot}15$. We thus expect that most FM clusters are separated for lower values of x but gradually merge to form larger clusters as x increases in the range of x studied. FM clusters will eventually form an infinite cluster, which may be the case with $x \geq 0{\cdot}15$; the transition to a rhombohedral structure (Fig. 2) might be an indication of the formation of an infinite cluster of the isotropic FM phase. It is noted that, according to the above picture, AF regions are predicted to survive in the rhombohedral phase ($x \geq 0{\cdot}15$). This is consistent with the recent pulsed neutron diffraction study by Louca *et al.* (1997), which detected the coexistence of short and long Mn–O bonds in $La_{1-x}Sr_xMnO_3$ even for $x > 0{\cdot}175$, where the material shows metallic conductivity below T_c and the average crystal structure is rhombohedral.

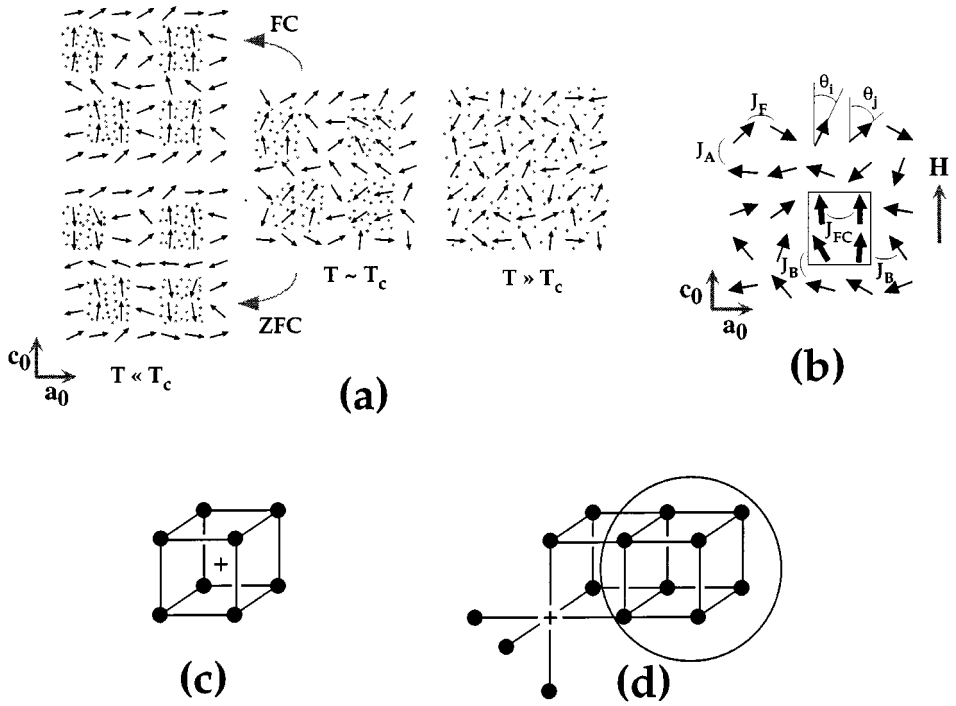

Fig. 10. (*a*) Schematic diagrams showing spin configurations and hole distributions at low temperature (left), near T_c (centre) and at high temperature (right). The density of grey dots is a measure of hole density. (*b*) 2D square lattice consisting of a 2×2 ferromagnetic cluster (surrounded by a square) embedded in an antiferromagnetic matrix. Various exchange interactions assumed in the Monte Carlo simulations are indicated. Local crystal structure around (*c*) La vacancy and (*d*) Mn vacancy. The filled circles (•) indicate Mn ions and the crosses (×) denote vacancies. La ions are omitted for clarity.

In $LaMnO_{3+\delta}$, cation vacancies occur on both the La and Mn sites (Kuo *et al*. 1989; Van Roosmalen *et al*. 1994). The FM clusters around the La vacancies and those around the Mn vacancies may be different in nature as the following considerations suggest. In the case of a La vacancy, the eight Mn ions surrounding the vacancy are crystallographically and electrostatically equivalent (Fig. 10*c*). The conditions for the double exchange interaction, the presence of neighbouring Mn^{3+}–Mn^{4+} pairs and degeneracy of the two configurations Mn^{3+}–Mn^{4+} and Mn^{4+}–Mn^{3+}, will then be satisfied locally, forming an FM cluster in which the e_g electrons are delocalised. Around an Mn vacancy, on the other hand, no neighbouring pair of Mn ions is equivalent; for example, the eight Mn ions indicated by the circle in Fig. 10*d* are each not equivalent, and the double exchange interaction would be weakened. In this case, it may be energetically favourable to localise the three holes among the six Mn sites next to the vacancy where the Coulomb potential is the lowest. We expect the formation of a FM cluster even in this case, since static Jahn–Teller distortion will be suppressed around the vacancy due to the presence of non-Jahn–Teller Mn^{4+} ions and the vacancy itself; without static orbital ordering, the exchange interactions are ferromagnetic not only between Mn^{3+}–Mn^{4+} pairs but also between Mn^{3+}–Mn^{3+}

pairs (Goodenough 1963). Thus, in the following qualitative discussion, we treat La and Mn vacancies indiscriminately, assuming the formation of a FM cluster around each vacancy. (This assumption is probably not justified for higher vacancy concentrations, as discussed later in this section.)

On the basis of the TPEC model, the hole distribution and the spin configuration for smaller x are expected to vary with temperature as schematically shown in Fig. 10*a*. The diagrams represent a cross section of the a_0c_0 plane, where a_0 and c_0 are the crystallographic axes of the basic perovskite unit cell; the grey dots show the distribution of holes and the arrows indicate the directions of Mn spins. [It is well established that the magnetisation easy direction in the AF phase is along the orthorhombic b-axis (Matsumoto 1970; Moussa *et al.* 1996); the horizontal component of each arrow should therefore be identified as the spin component along the b-axis.] At high temperatures ($T \gg T_c$) the hole distribution will be approximately uniform and the spin orientation will be roughly random, as in the right-hand diagram of Fig. 10*a*. As the temperature decreases towards T_c, the holes tend to concentrate in regions near the cation vacancies to take advantage of the low Coulomb potential. Inside the hole-rich regions, the spins are coupled ferromagnetically through strong double exchange (DE) interactions, thus forming FM spin clusters (middle diagram of Fig. 10*a*). The formation of FM spin clusters accounts for the curvature of the hysteresis loops above T_c (Fig. 8) and the upward deviation of the $1/\chi$ versus T curve from a straight line (Fig. 3). The spins in the hole-free matrix will then order antiferromagnetically as the temperature is lowered through T_c (T_N), resulting in the freezing of the FM spin clusters. This process corresponds to the sharp decrease in $1/\chi$ observed for smaller x in Fig. 3. If the sample is cooled in a field, the FM clusters will be frozen so that the spins in the clusters orient along the field, as in the upper-left diagram of Fig. 10*a*. If, on the other hand, the sample is cooled in zero field, there will be no preference for the orientation of FM clusters and once the FM clusters are frozen (lower-left diagram of Fig. 10*a*) the nett magnetisation will be zero. Thus, T_0 and T_c for smaller x ($\lesssim 0{\cdot}12$) may be interpreted as the temperatures at which the AF ordering of the hole-free matrix starts and completes, respectively. Since the AF matrix is diluted more as the density of FM clusters increases with x, the AF ordering temperature, and hence T_0 and T_c, decrease with increasing x (Fig. 4).

With an increase in x, the separation between FM clusters decreases. (At the same time, some of the FM clusters will merge to form larger clusters.) This allows neighbouring FM clusters to interact via the intervening spins in the AF matrix: a FM cluster cants the surrounding spins in the AF matrix through superexchange interactions, which results in effective unidirectional anisotropy for a second FM cluster (see below). In this case, magnetic ordering no longer depends on the AF ordering of the matrix. The inter-cluster interaction becomes stronger as the separation between FM clusters decreases with increasing x, resulting in an increase in T_c. As x increases further, FM clusters eventually merge to form an infinite cluster.

To visualise spin configurations and demagnetisation processes at low temperature, we have carried out Monte Carlo simulations, applying a 2D XY model to a square lattice as shown in Fig. 10*b*, which again represents the spin configuration in the a_0c_0 plane. We considered systems consisting of a periodic array of 2×2

FM clusters embedded in an AF matrix, and used the following Hamiltonian to determine their spin configurations:

$$H = -\sum J_{ij} S_i S_j \cos(\theta_i - \theta_j) - H \sum S_i \cos\theta_i - K \sum S_i \sin^2\theta_i \,, \tag{1}$$

where J_{ij} is the exchange interaction between nearest-neighbour spins S_i and S_j, θ_i is the angle between the c_0 axis and S_i, H is the magnetic field applied along the c_0 axis, and K is the crystalline anisotropy. Thus, the first, second and third terms of the right-hand side of (1) represent the exchange energy, Zeeman energy and crystalline anisotropy energy, respectively. Here J_{ij} inside the FM clusters was assumed to be positive ($J_{\mathrm{FC}} > 0$), while J_{ij} within the AF matrix was assumed to be anisotropic, i.e. positive along the a_0 axis ($J_{\mathrm{F}} > 0$) and negative along the c_0 axis ($J_{\mathrm{A}} < 0$). Here J_{ij} across the FM–AF phase boundaries was assumed to be positive ($J_{\mathrm{B}} > 0$) for both directions, since across the boundary there should be no static orbital ordering, which is necessary for anisotropic superexchange interactions (Goodenough 1963). Here K was assumed to be zero inside the FM clusters, considering the soft magnetic behaviour of the optimally doped FM phase. The numerical parameters used in the simulations are $J_{\mathrm{FC}} = 5$, $J_{\mathrm{F}} = J_{\mathrm{B}} = 1$, $J_{\mathrm{A}} = -1$ and $K = 0{\cdot}2$ (within the AF matrix), all in the unit of kT, and $T = 0{\cdot}1$. We chose these parameters, which satisfy the relationship $J_{\mathrm{FC}} \gg J_{\mathrm{F}} \sim |J_{\mathrm{A}}| \gg K$, based on the values determined experimentally: $J_{\mathrm{FC}} = 27{\cdot}6$ K for $La_{0{\cdot}7}Pb_{0{\cdot}3}MnO_3$ (Perring *et al.* 1996) and $J_{\mathrm{F}} = 9{\cdot}6$ K, $J_{\mathrm{A}} = -6{\cdot}7$ K and $K = 1{\cdot}92$ K for $LaMnO_3$ (Moussa *et al.* 1996). The simulations were carried out on a computer by progressively updating the spin configuration using a standard Metropolis algorithm. Lattice sizes ranging between 12×12 and 20×20 were used with periodic boundary conditions. To obtain a demagnetisation curve, H was swept from 1 to -1 in steps of $0{\cdot}05$, and the magnetisation M was recorded after 1000 MCS were performed at each value of H.

Demagnetisation curves thus obtained are shown in Fig. 11 for three different FM cluster densities. In the graph, p indicates the period with which the FM clusters are placed (a large p thus corresponds to a smaller cluster density and hence a smaller x), and M is normalised to the value for full alignment of the spins along the field direction. It can be seen that as the cluster density increases with decreasing p, M_{s} increases, H_{c} decreases and the ratio $M(H = 1)/M(H = 0)$ decreases (i.e. magnetisation becomes easier to saturate). These features, in qualitative agreement with the experimental results (Figs 5 and 8), are well understood in terms of the diagrams below the graph in Fig. 11, which show snapshots of the spin configurations at different points in the demagnetisation curves for $p = 3$ and 5; the bold and thin arrows denote spins in the FM clusters and the AF matrix, respectively, with the overall sublattice magnetisations indicated below each diagram.

At the remanence ($H = 0$), the spins in the AF matrix tend to align horizontally with the spin directions alternating along the c_0 axis, because of the anisotropic exchange interactions and the crystalline anisotropy. The spins within the FM clusters are almost parallel to one another and point along the c_0 axis, i.e. the direction perpendicular to the magnetisation easy direction of the AF phase, with a certain degree of wobbling due to thermal agitation. This is because

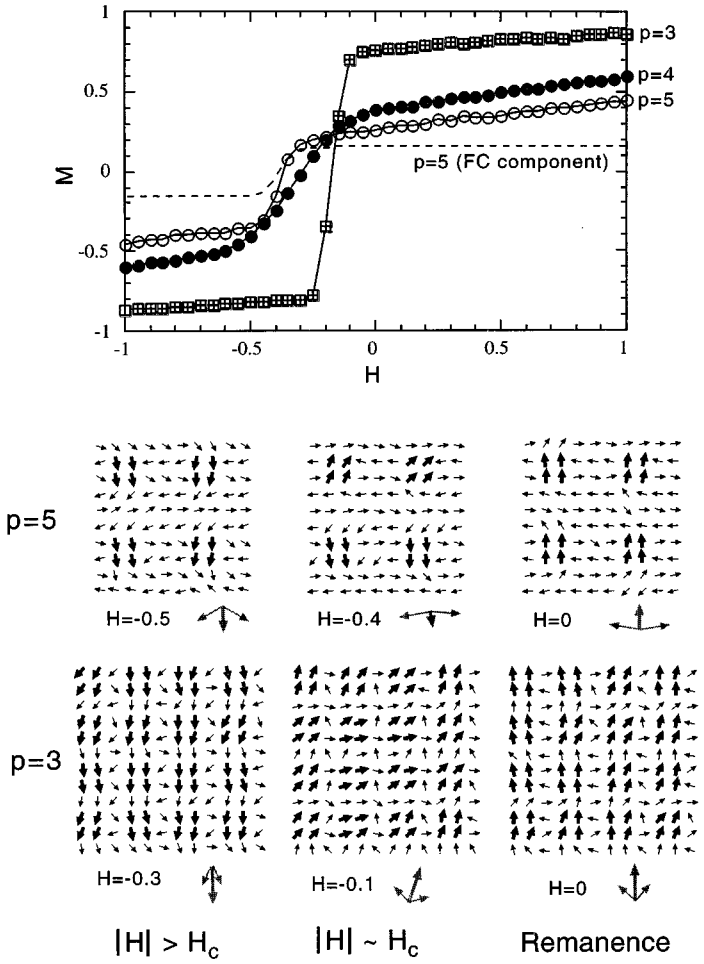

Fig. 11. Upper graph: Demagnetisation curves obtained from Monte Carlo simulations. Results for three different FM cluster densities are shown. Here p indicates the period with which the FM clusters are placed in the AF matrix. The dashed line shows the contribution of the FM clusters to the total magnetisation for $p = 5$. Lower diagrams: Snapshots of spin configurations at various points of the demagnetisation curve for two different FM cluster densities. Bold and thin arrows indicate spins in the FM clusters and those in the AF matrix, respectively.

the exchange interactions within the FM clusters (J_{FC}) are much stronger than those in the AF phase (J_{F} and J_{A}) and across the phase boundary (J_{B}), and the cost in exchange energy arising from the frustration at the FM–AF phase boundaries is minimised with these configurations. The spins in the AF phase near the FM clusters cant towards the same direction as that of the FM clusters because of the exchange coupling of the two phases through J_{B}. The canting angle increases with cluster density, since the spin orientations in the AF matrix are influenced more by that in the FM clusters. Thus, in addition to an increase in the number of almost fully polarised spins in the FM clusters, an increase in the spin canting angle in the AF matrix also contributes to the increase in M_{s};

this explains why M_s is not proportional to x but increases more abruptly in the range $0{\cdot}08 \leq x \leq 0{\cdot}15$ (Fig. 6).

It is noted that at $H = 0$ all the states in which the FM clusters are parallel to the c_0 axis are roughly degenerate regardless of the number of FM clusters flipped, as illustrated schematically in Fig. 12*a*. Which state is realised depends on the previous history: if the system is cooled in a positive field or if the field is reduced from a large positive value, then state I, in which all the FM clusters point upward, will be realised; if, on the other hand, the system is cooled in zero field, then state II, in which half of the FM clusters point downward, will be realised and the nett magnetisation will be zero.

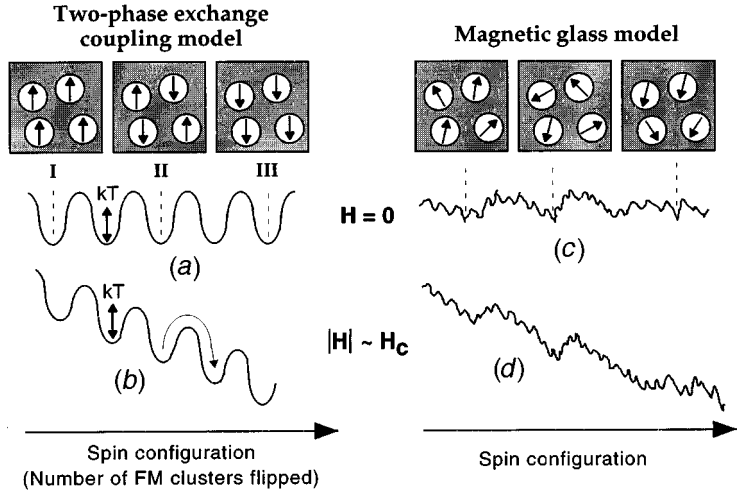

Fig. 12. Schematic energy level diagrams for the two-phase exchange coupling (TPEC) model proposed in this paper and for the magnetic glass (MG) model (Töpfer and Goodenough 1997; Ju and Sohn 1997).

Under a negative H, the state in which all the FM clusters point upward (state I in Fig. 12) becomes energetically unfavourable as compared with the one in which all the FM clusters point downward (state III). For a smaller $|H|$, however, magnetisation reversal does not take place, because the FM clusters are self-trapped in the exchange fields they produced in the AF matrix surrounding them; the configurations at $H = 0$ (Fig. 11) are metastable and a certain amount of energy is required to flip the FM clusters. The situation is analogous to that of small dielectric polarons, which are self-trapped in the electrostatic fields they produced by distorting the surrounding lattice.

As $|H|$ increases, the potential barrier for the flipping of FM clusters is lowered as illustrated in Fig. 12*b*, and when it becomes comparable to the thermal energy the FM clusters flip, corresponding to the steep decrease in M near H_c. The lower H_c for a higher cluster density is attributed to the following two factors. First, the number of spins in the AF matrix per FM cluster decreases with increasing cluster density. Since the coercivity originates in the crystalline anisotropy of the AF phase, the reduction in the number of the spins in the AF phase results in an easier rotation of FM clusters, and hence a lower H_c. Second,

the spin canting angle in the AF matrix increases with cluster density, as already mentioned. This reduces the effectiveness of the coercivity mechanism, because once a spin in one of the AF sublattices rotates past the c_0 axis ($\theta_i = 0$), both the crystalline anisotropy term and the Zeeman term favour further rotation, resulting in the loss of restoring force. [In the real materials the orthorombicity decreases with increasing x (Fig. 2), and the resultant decrease in crystalline anisotropy also contributes to the decrease in H_c.]

From the diagrams in Fig. 11, the magnetisation at a given H consists of two contributions: one from the FM clusters (M_{FC}), which are almost fully polarised either upward or downward except near H_c, and the other from the canted spins in the AF matrix (M_{AM}). This is demonstrated more quantitatively in the graph of Fig. 11, where M_{FC} is plotted with a dashed line for $p = 5$. It can be seen that M_{FC} is essentially independent of H except near H_c where the magnetisation changes sign. The difference between the two curves accounts for $|M_{AM}|$, which increases as the spin canting angle increases with $|H|$. As the cluster density increases, the ratio M_{AM}/M_{FC} decreases and the H dependence of M becomes smaller.

We emphasise here that the TPEC model is distinct from the magnetic glass (MG) model (Töpfer and Goodenough 1997; Ju and Sohn 1997), although both are based on an FM–AF two-phase picture. In the latter model, it is assumed that the FM clusters are frozen in the AF matrix with their spin directions pointing towards *randomly* distributed local easy directions, as schematically shown on the right of Fig. 12. While the MG model also explains some of the experimental observations, e.g. the small ZFC magnetisations at low temperature (Fig. 3), the lack of saturation of magnetisation for small x (Figs 5 and 8) and the large temperature dependence of H_c (Fig. 7), we believe that the TPEC model is more appropriate in describing the magnetic structure of $LaMnO_{3+\delta}$ in the low-x region. The strongest evidence in favour of the TPEC model is the minor hysteresis loops presented in Fig. 9. In the MG model, the energies of the metastable states distribute almost continuously, and the energy level landscape should consist of potential barriers having a wide range of heights, as illustrated in Figs 12*c* and 12*d*. At a finite temperature, then, the system would be able to relax towards a lower-energy state by jumping over the potential barriers comparable to or smaller than kT, and magnetisation would always contain an irreversible component. As can be seen in Fig. 9, however, the magnetisation of the sample with $x = 0{\cdot}08$ is almost completely reversible even under negative fields ($|H| \leq 1$ kOe), indicating the absence of lower potential barriers. The small time dependence of magnetisation except near H_c (Fig. 9) and the lack of temperature dependence of remanence at low temperature (Fig. 8) also suggest deeper potential wells, as in Figs 12*a* and 12*b*, thus favouring the TPEC model; in fact, in amorphous Dy–Cu alloy, a typical spin-glass system, a large time dependence of magnetisation and exponential temperature dependence of remanence have been observed (Coey *et al.* 1981).

We now discuss the step-like features observed in the hysteresis loops at 2 K for smaller x (Fig. 8). We provide four possible explanations of this anomalous behaviour:

(1) In discussing magnetisation reversal, we used the simplified energy level diagrams shown in Figs 12*a* and 12*b*, which consist of a series of potential

wells with equal depths; that is, we assumed that all the states in which the FM clusters are parallel to the c_0 axis are degenerate. Strictly speaking, however, this is not correct even for idealised periodic lattices like those in Fig. 11, since the spin configuration in the AF matrix depends on the orientations of the FM clusters. Let us consider a state in which neighbouring pairs of FM clusters orient antiparallel, as in state II in Fig. 12. In this state the spins in the regions between neighbouring FM clusters are frustrated with respect to the direction of spin canting. This results in a higher total exchange energy than in the states in which all the FM clusters align parallel (e.g. states I and III in Fig. 12). The frustration, on the other hand, reduces the average spin canting angle in the AF matrix, thus decreasing the total crystalline anisotropy energy. Considering that J_{ij} is much larger than K and that the coercivity mechanism is more effective for a smaller spin canting angle in the AF matrix, it is expected that the states in which half of the FM clusters are flipped ($M \sim 0$) are higher in energy but more stable than the states in which all the FM clusters align parallel ($M \sim M_\mathrm{s}$); that is, in Fig. 12*a* the bottom of the potential well is higher for state II than for states I and III, but the potential well for state II is deeper than those for states I and III. Trapping of the system in these 'more stable' metastable states could result in the interruption of magnetisation reversal near $M = 0$. [Step-like features indeed showed up in some of the simulated demagnetisation curves for lower cluster densities ($p \geq 6$).]

(2) In the TPEC model, coercivity originates in the crystalline anisotropy of the AF phase, which prevents free rotation of the spins in the (orthorhombic) *bc*-plane. However, the crystalline anisotropy alone cannot prevent coherent rotation of the whole spins about the *b*-axis, since it preserves the angle between each spin and the *b*-axis, and hence the crystalline anisotropy energy. What prevents such coherent rotation is the Dzyaloshinski–Moriya (DM) anisotropic exchange interaction given by $\Delta E = \boldsymbol{D}_{ij} \cdot (\boldsymbol{S}_i \times \boldsymbol{S}_j)$, where $\boldsymbol{S}_i$ and $\boldsymbol{S}_j$ are the spins in the two sublattices of the AF phase and the vector $\boldsymbol{D}_{ij}$ points to the *a*-axis in the case of $LaMnO_3$ (Goodenough 1963). For a given canting angle, the energy gain ΔE is maximum when $\boldsymbol{S}_i$ and $\boldsymbol{S}_j$ lie in the *bc*-plane so that $\boldsymbol{S}_i \times \boldsymbol{S}_j$ is parallel to $\boldsymbol{D}_{ij}$, and decreases as $\boldsymbol{S}_i$ and $\boldsymbol{S}_j$ rotate coherently about the *b*-axis; thus the spins in the AF phase, and those in the exchange-coupled FM phase, tend to be confined in the *bc*-plane. (This is a justification for the simulations on 2D lattices.) If $|H|$ exceeds a certain critical value, however, the DM interaction will be overcome and magnetisation reversal will occur through coherent rotation of the whole spins about the *b*-axis. Such a situation will be realised only at low temperature, since at high temperature, magnetisation reversal occurs through the flipping of individual FM clusters by thermal activation before $|H|$ exceeds the critical value.

(3) For smaller x, cation vacancies are fairly well separated from one another, and the FM clusters are expected to consist of small numbers of Mn atoms, e.g. Mn_8, corresponding to one perovskite unit cell, and Mn_{12}, corresponding to two perovskite unit cells. It is possible that the FM

clusters, having the same spin quantum numbers, flip through macroscopic quantum tunnelling at low temperature, resulting in step-like features in the hysteresis loop. Similar step-like features have been observed in the low-temperature hysteresis loops for Mn_{12}-ac, an organic compound containing superparamagnetic Mn_{12} clusters (Thomas *et al.* 1996). (Note that the origin of the uniaxial anisotropy that determines the magnetisation easy direction of the FM clusters is different between the two systems: in $LaMnO_{3+\delta}$ the anisotropy arises from exchange coupling to the AF phase, while in Mn_{12}-ac it arises purely from the symmetry of the crystal.)

(4) As the temperature decreases, the magnitude of H at which the flipping of FM clusters occurs increases, and the energy release involved in a change in magnetisation, $H\Delta M$, increases. This, combined with the decrease in the lattice specific heat with temperature, could induce avalanches of FM cluster flipping, resulting in large discrete jumps of magnetisation. Step-like features, similar to those in Fig. 8, have been observed in an amorphous Dy–Cu alloy and interpreted as arising from the Barkhausen effect in a sample containing about half a dozen domains (Coey *et al.* 1981). Unlike the hysteresis loops for the Dy–Cu alloy, however, the hysteresis loops for $LaMnO_{3+\delta}$ are always symmetrical (Fig. 8) regardless of whether the sample is field-cooled or zero-field-cooled, and the locations of the steps are reproducible, as already mentioned.

At present, we are unable to pinpoint the exact cause of the step-like features. (It is possible that two or more of the above mechanisms are simultaneously at work.) Further investigation is needed to clarify it.

Finally, we discuss the difference between the $LaMnO_{3+\delta}$ system and cation-substituted systems $La_{1-x}A_xMnO_3$, where A is a divalent cation such as Ca, Sr, Ba and Pb. Although in both cases ferromagnetism evolves in a qualitatively similar manner as holes are introduced in the AF parent compound $LaMnO_3$, there are three important differences. First, in $LaMnO_{3+\delta}$ the cation vacancies that work as acceptors have an effective charge of $-3e$, whereas in $La_{1-x}A_xMnO_3$ the A^{2+} ions have an effective charge of $-e$. As a result, the holes are more strongly bound to the acceptors in the former than in the latter. Second, for the same hole concentration the vacancy concentration in $LaMnO_{3+\delta}$ is three times the A concentration in $La_{1-x}A_xMnO_3$. This, combined with the first factor, results in a larger spatial variation of Coulomb potential in the former than in the latter. Third, the concentration of Mn ions, which support both electrical conductivity and ferromagnetism, decreases as δ increases in $LaMnO_{3+\delta}$, while the Mn sublattice remains intact in $La_{1-x}A_xMnO_3$. All these three factors favour the localisation of FM clusters in $LaMnO_{3+\delta}$. This is a possible reason why metallic conductivity does not show up (Ritter *et al.* 1997) or is observed only at rather high hole concentrations ($0{\cdot}28 < x < 0{\cdot}36$) (Töpfer and Goodenough 1997) in $LaMnO_{3+\delta}$, while an insulator–metal transition occurs at $x \sim 0{\cdot}175$ in $La_{1-x}Sr_xMnO_3$ (Urushibara *et al.* 1995). The above three factors could also explain the spin-glass-like behaviour observed in $LaMnO_{3+\delta}$ in the high hole concentration region ($x > \sim 0{\cdot}3$) (Töpfer and Goodenough 1997). With a stronger tendency of the holes towards localisation, the probability of two holes occupying neighbouring Mn sites will increase significantly as δ increases. The

exchange interactions between Mn^{4+}–Mn^{4+} pairs are antiferromagnetic so that they compete with the FM interactions between Mn^{3+}–Mn^{4+} and Mn^{3+}–Mn^{3+} pairs. The resultant magnetic disorder will be further enhanced by the presence of Mn vacancies. The magnetic structure in the high hole concentration region will be best described by the magnetic glass model as proposed by Töpfer and Goodenough (1997).

The following are the main conclusions of the present work.

(1) The low-temperature magnetic structure of $LaMnO_{3+\delta}$ having low hole concentrations ($x = 2\delta \leq 0{\cdot}15$) is described as a mixture of a hole-free antiferromagnetic (AF) phase and a ferromagnetic (FM) phase with the optimal hole concentration ($x \sim 0{\cdot}25$–$0{\cdot}3$), and not as a single AF phase with canted spins.
(2) Clusters of the FM phase, most likely to be formed near cation vacancies, are embedded in a matrix of the AF phase.
(3) There are two contributions to magnetisation: polarisation of FM clusters and spin canting in the AF matrix towards the field direction.
(4) Coercivity arises from the exchange coupling of the two phases, which sets up effective uniaxial anisotropy for the FM clusters.

References

Asamitsu, A., Moritomo, Y., Kumai, R., Tomioka, Y., and Tokura, Y. (1996). *Phys. Rev.* B **54**, 1716.

Chahara, K., Ohno, T., Kasai, M., and Kozono, Y. (1993). *Appl. Phys. Lett.* **63**, 1990.

Coey, J. M., McGuire, T. R., and Tissier, B. (1981). *Phys. Rev.* B **24**, 1261.

de Gennes, P.-G. (1959). *Phys. Rev.* **118**, 141.

Goodenough, J. B. (1955). *Phys. Rev.* **100**, 564.

Goodenough, J. B. (1963). 'Magnetism and the Chemical Bond' (Interscience: New York).

Hennion, M., Moussa, F., Rodriguez-Carvajal, J., Pinsard, L., and Revcolevschi, A. (1997). *Phys. Rev.* B **56**, R497.

Ju, H. L., and Sohn, H. (1997). *J. Magn. Magn. Mater.* **167**, 200.

Kawano, H., Kajimoto, R., Kubota, M., and Yoshizawa, H. (1996). *Phys. Rev.* B **53**, 2202.

Kuo, J. H., Anderson, H. U., and Sparlin, D. M. (1989). *J. Solid State Chem.* **83**, 52.

Kusters, R. M., Singleton, J., Keen, D. A., McGreevy, R., and Hayes, W. (1989). *Physica* B **155**, 362.

Louca, D., Egami, T., Brosha, E. L., Röder, H., and Bishop, A. R. (1997). *Phys. Rev.* B **56**, R8475.

Matsumoto, G. (1970). *J. Phys. Soc. Jpn* **29**, 606.

Moussa, F., Hennion, M., Rodriguez-Carvajal, J., Moudden, H., Pinsard, L., and Revcolevschi, A. (1996). *Phys. Rev.* B **54**, 15149.

Perring, T. G., Aeppli, G., Hayden, S. M., Carter, S. A., Remeika, J. P., and Cheong, S.-W. (1996). *Phys. Rev. Lett.* **77**, 711.

Ritter, C., Ibbarra, M. R., De Teresa, J. M., Algarabel, P. A., Martquina, C., Blasco, J., Oseroff, S., and Cheong, S.-W. (1997). *Phys. Rev.* B **56**, 4558.

Searle, C. W., and Wang, S. T. (1970). *Can. J. Phys.* **48**, 2023.

Thomas, L., Lionti, F, Ballou, F., Gatteschi, D., Sessoli, R., and Barbara, B. (1996). *Nature* **383**, 145.

Töpfer, J., and Goodenough, J. B. (1997). *J. Solid State Chem.* **130**, 117.

Urushibara, A., Moritomo, Y., Arima, T., Asamitsu, A., Kido, G., and Tokura, Y. (1995). *Phys. Rev.* B **51**, 14103.

Van Roosmalen, J. A. M., Cordfunke, E. H. P., Helmholdt, R. B., and Zandbergen, H. W. (1994). *J. Solid State Chem.* **110**, 100.

Van Roosmalen, J. A. M., van Vlaanderen, P., Cordfunke, E. H. P., Ijdo, W. L., and Ijdo, D. J. W. (1995). *J. Solid State Chem.* **114**, 516.

Von Helmolt, R., Wecker, J., Holzapfel, B., Schultz, L., and Samwer, K. (1993). *Phys. Rev. Lett.* **71**, 2331.
Wollan, E. O., and Koehler, W. C. (1955). *Phys. Rev.* **100**, 545.
Yao, T., Ito, T., and Kokubo, T. (1995). *J. Mater. Res.* **10**, 1079.
Zener, C. (1951). *Phys. Rev.* **82**, 403.

Manuscript received 5 August, accepted 19 October 1998